

# CONSTRAINTS ON THE SPACETIME GEOMETRY AROUND 10 STELLAR-MASS BLACK HOLE CANDIDATES FROM THE DISK'S THERMAL SPECTRUM

LINGYAO KONG, ZILONG LI, AND COSIMO BAMBI<sup>a</sup>

Center for Field Theory and Particle Physics & Department of Physics, Fudan University, 200433 Shanghai, China

*Draft version October 10, 2014*

## ABSTRACT

In a previous paper, one of us has described a code to compute the thermal spectrum of geometrically thin and optically thick accretion disks around generic stationary and axisymmetric black holes, which are not necessarily of the Kerr type. As the structure of the accretion disk and the propagation of electromagnetic radiation from the disk to the distant observer depend on the background metric, the analysis of the thermal spectrum of thin disks can be used to test the actual nature of black hole candidates. In this paper, we consider the 10 stellar-mass black hole candidates for which the spin parameter has been already estimated from the analysis of the disk's thermal spectrum and under the assumption of the Kerr background, and we translate the measurements reported in the literature into constraints on the spin parameter–deformation parameter plane. The analysis of the disk's thermal spectrum can be used to estimate only one parameter of the geometry close to the compact object, and therefore it is not possible to get independent measurements of both the spin and the deformation parameters. The constraints obtained here will be used in combination with other measurements in future work, with the final goal to break the degeneracy between the spin and possible deviations from the Kerr solution and thus test the Kerr black hole hypothesis.

*Subject headings:* accretion, accretion disks — black hole physics — gravitation — X-rays: binaries

## 1. INTRODUCTION

General relativity makes very clear predictions about the properties of the spacetime geometry around a black hole (BH). According to the no-hair theorem (Carter 1971; Robinson 1975; Chruściel et al. 2012), 4-dimensional uncharged BHs are only described by the Kerr solution, which is completely specified by two parameters, associated respectively to the mass  $M$  and the spin angular momentum  $J$  of the compact object.  $a_* = J/M^2$  is the spin parameter and a Kerr BH must have  $|a_*| \leq 1$ . For  $|a_*| > 1$ , there is no event horizon and there is a number of theoretical arguments suggesting that such super-spinning Kerr objects can unlikely be relevant in astrophysics (Dotti et al. 2008; Pani et al. 2010; Barausse et al. 2010; Giacomazzo et al. 2011).

Astronomical observations have discovered at least two classes of BH candidates. Dark and compact objects in X-ray binary systems with a mass  $M \approx 5 - 20 M_\odot$  (Remillard & McClintock 2006) are too heavy to be relativistic stars made of neutrons or quarks for plausible matter equations of state (Rhoades & Ruffini 1974; Kalogera & Baym 1996). The supermassive BH candidates at the center of every normal galaxy have a mass  $M \sim 10^5 - 10^9 M_\odot$  (Kormendy & Richstone 1995) and they turn out to be too massive, compact, and old to be clusters of non-luminous bodies, because the cluster lifetime due to physical collisions and evaporation would be shorter than the age of these systems (Maoz 1998). For both stellar-mass and supermassive BH candidates, there is no evidence of electromagnetic radiation emitted by their surface, which may be interpreted as an indication for the presence of an event/apparent horizon (Narayan & Heyl 2002; McClintock et al. 2004; Narayan & McClintock 2008; Broderick et al. 2009). In the end, all these objects are thought to be the Kerr BHs of general relativity simply because they cannot be explained otherwise without introducing new physics.

Despite this body of indirect evidence, there is no indication that the spacetime geometry around BH candidates is described by the Kerr metric. The Kerr BH hypothesis entirely relies on the validity of standard physics. The no-hair theorem might be avoided by a number of ways, such as by considering exotic forms of matter, non-stationary solutions, or non-trivial extensions of general relativity. It is therefore of extreme importance to experimentally test the Kerr nature of astrophysical BH candidates and, thanks to the progresses in the last decade in the understanding of the accretion processes and in the observational facilities, such a possibility is not out of reach any more [for a review, see e.g. Bambi (2011, 2013b)]. This goal can be achieved by extending the techniques that have been developed to estimate the spin parameter of BH candidates under the assumption that they are of the Kerr type. The compact object is now specified by a mass  $M$ , a spin parameter  $a_*$ , and at least one deformation parameter, which measures possible deviations from the Kerr geometry. One then computes the observational features in this more general background. The comparison of the theoretical predictions with the observational data is now used to estimate both the spin and the deformation parameters. If one finds a vanishing deformation parameter, the Kerr BH hypothesis is verified. If the observational data point out a non-vanishing deformation parameter, the Kerr nature of astrophysical BH candidates is questioned. However, even assuming to have the correct astrophysical model and all the systematic effects under control, there is usually a strong correlation between the estimate of the spin and of the deformation parameter, so the

<sup>a</sup> Corresponding author: bambi@fudan.edu.cn

final result is a constraint on the spin parameter–deformation parameter plane (Bambi & Barausse 2011; Krawczynski 2012; Bambi 2013a, 2014b). Only in presence of excellent data, not available today and probably not even in the near future, it might be possible to solve such a fundamental degeneracy between the spin and possible deviations from the Kerr geometry. The strategy is therefore to combine different measurements of the same object and break this degeneracy (Tsukamoto et al. 2014; Bambi 2014c). With a single measurement, we can only rule out some BH alternatives with very specific features, like some exotic compact objects without event horizon (Bambi & Malafarina 2013; Joshi et al. 2014) and some wormholes (Bambi 2013c), or constrain the deformation parameter in classes of non-Kerr BHs that can mimic fast-rotating Kerr BHs only for a restricted range of the spin and of the deformation parameters (Bambi 2014a).

At present, the most robust technique to probe the spacetime geometry around stellar-mass BH candidates is probably the continuum-fitting method; that is, the analysis of the thermal spectrum of geometrically thin and optically thick accretion disks (Zhang et al. 1997). In the case of Kerr BHs, the thermal spectrum of thin accretion disks depends on 5 free parameters; that is, the BH mass  $M$ , the BH spin parameter  $a_*$ , the mass accretion rate  $\dot{M}$ , the BH distance  $d$ , and the inclination angle  $i$  of the disk with respect to the line of sight of the distant observer. As put forward in Zhang et al. (1997), if we have independent measurements of  $M$ ,  $d$ , and  $i$ , the analysis of the disk’s thermal spectrum can provide an estimate of  $a_*$  and  $\dot{M}$ . This approach has been extensively discussed in the literature, its assumptions and limitations well investigated and tested at both theoretical and observational level, and up to now the technique has been used to estimate the spin parameter of about 10 stellar-mass BH candidates (Li et al. 2005; McClintock et al. 2011, 2013). The continuum-fitting method cannot be used in the case of supermassive objects because the disk’s temperature goes like  $M^{-0.25}$ , and for  $M \sim 10^5 - 10^9 M_\odot$  the peak falls in the optical/UV range, where dust absorption prevents good observations. The analysis of the disk’s thermal spectrum can be naturally extended to non-Kerr spacetimes (Bambi & Barausse 2011; Bambi 2012e).

In the present paper, we will use the code described in Bambi (2012e) to constrain the spin parameter and the deformation parameter of the 10 stellar-mass BH candidates in X-ray binary systems for which the continuum-fitting method has already been used by other authors to get an estimate of the spin parameter under the assumption that these objects are Kerr BHs. Our code is based on a ray-tracing approach and includes all the special and general relativistic effects. The natural way to obtain these constraints would be to start from the raw data and repeat the complete data analysis for each object, with the sole difference that the thermal spectrum is now computed in a more general metric that includes the Kerr solution as special case. While this would be surely the correct way to proceed, here we will employ a simplified analysis in which, significantly reducing the time of the analysis as well as the complications related to a large number of systematic effects, we will not lose any important information. The idea is to compare the Kerr spectra with the spin parameters reported in the literature with the spectra computed in our generic spacetime with a possible non-vanishing deformation parameter. The approach works because the thermal spectrum of a thin disk around a non-Kerr BH with a certain spin and deformation parameters is extremely similar to the one around a Kerr BH with different spin and that remains true even for quite large deviations from the Kerr solution. In other words, it is impossible to distinguish a Kerr BH and a non-Kerr BH from the sole analysis of the disk’s thermal spectrum (Bambi 2012e, 2014a) and therefore we can assume as reference spectrum the one of a Kerr BH with the spin reported in the literature. This approach significantly simplify our job because we can just focus our attention on the role of the spacetime metric, assuming that all the astrophysical effects and the instrumental issues have been already properly taken into account in the previous studies. Our work is the first step of a project that aims at testing the Kerr nature of BH candidates: the measurements reported in the present paper will be combined with other observations to try to break the degeneracy between the spin and the deformation parameters. We note that the use of the measurements from the continuum-fitting method and their combinations with other observations have already been studied in previous papers (Bambi 2012b,c,d). However, those constraints were obtained with some simplifications that, as we will show here, provide the correct measurement in the limit of slow-rotating BHs and small inclination angles. Here we will remove such a set of simplifications.

The content of the paper is as follows. In Section 2, we review the calculations of the thermal spectrum of geometrically thin and optically thick accretion disks around generic stationary and axisymmetric BHs. In Section 3, we present our approach and, in Section 4, we find the constraints on the spin parameter–deformation parameter plane for each of the 10 stellar-mass BH candidates for which a spin measurement from the disk’s thermal spectrum has been reported in the literature. Summary and conclusions are reported in Section 5. Throughout the paper, we use units in which  $G_N = c = 1$ , unless stated otherwise.

## 2. THERMAL SPECTRUM OF THIN DISKS

The calculation of the thermal spectrum of a thin disk around a BH consists of two parts: the calculation of the disk structure and the one of the propagation of the radiation from the disk to the observer, see e.g. Li et al. (2005) and references therein. For the first part concerning the disk structure, we adopt the Novikov-Thorne model (Novikov & Thorne 1973; Page & Thorne 1974), which is the relativistic generalization of the Shakura-Sunyaev one (Shakura & Sunyaev 1973) and describes geometrically thin and optically thick accretion disks in generic stationary, axisymmetric, and asymptotically flat spacetimes. The model relies on a set of assumptions, whose validity has been tested by a number of theoretical and observational studies (McClintock et al. 2013). These assumptions are thought to hold in the case of geometrically thin and optically thick accretion disks, and the observational criterion to select sources with similar disks is that the accretion luminosity must be in the range  $\sim 8 - 20\%$  the Eddington luminosity. The disk is supposed

to be on the equatorial plane and the particles of the disk move on nearly geodesic circular orbits. From the conservation laws for the rest-mass, the energy, and the angular momentum, one obtains the equations governing the radial structure of the disk (Page & Thorne 1974). The mass accretion rate  $\dot{M}$  is independent of the time and the radial coordinate, and the time-averaged energy flux is

$$\mathcal{F}(r) = \frac{\dot{M}}{4\pi M^2} F(r), \quad (1)$$

where

$$F(r) = -\frac{\partial_r \Omega}{(E - \Omega L_z)^2} \frac{M^2}{\sqrt{-G}} \int_{r_{\text{in}}}^r (E - \Omega L_z) (\partial_\rho L_z) d\rho. \quad (2)$$

$\Omega$ ,  $E$ , and  $L_z$  are, respectively, the angular velocity  $d\phi/dt$  of equatorial circular geodesics, the conserved specific energy, and the conserved axial component of the specific angular momentum.  $G = -\alpha^2 g_{rr} g_{\phi\phi}$  is the determinant of the near equatorial plane metric in cylindrical coordinates, and  $\alpha^2 = g_{t\phi}^2/g_{\phi\phi} - g_{tt}$  is the lapse function.  $r_{\text{in}}$  is the radial coordinate of the inner edge of the accretion disk and the key-point for what follows is that  $r_{\text{in}}$  is assumed to coincide with the innermost stable circular orbit (ISCO). The calculation of  $\Omega$ ,  $E$ , and  $L_z$  in a generic stationary and axisymmetric spacetime can be found, for instance, in Appendix B of Bambi & Barausse (2011).

As the disk is in thermal equilibrium, it is possible to define an effective temperature  $T_{\text{eff}}(r) = [\mathcal{F}(r)/\sigma]^{1/4}$ , where  $\sigma$  is the Stefan-Boltzmann constant. In the case of stellar-mass BH candidates, the temperature of the disk can be at the level of  $10^7$  K near its inner edge and therefore non-thermal effects have to be taken into account. That can be done by introducing the color temperature  $T_{\text{col}}(r) = f_{\text{col}} T_{\text{eff}}$ , where  $f_{\text{col}}$  is usually referred as color factor or hardening factor, and the local specific intensity of the radiation emitted by the disk can be written as

$$I_e(\nu_e) = \frac{2h\nu_e^3}{c^2} \frac{1}{f_{\text{col}}^4} \frac{\Upsilon}{\exp\left(\frac{h\nu_e}{k_B T_{\text{col}}}\right) - 1}. \quad (3)$$

Here,  $h$ ,  $c$ , and  $k_B$  are, respectively, the Planck constant, the speed of light, and the Boltzmann constant.  $\nu_e$  is the photon frequency in the rest frame of the emitter.  $\Upsilon$  is a function of  $\xi$ , the angle between the wavevector of the photon emitted by the disk and the normal of the disk surface. In the case of isotropic emission,  $\Upsilon = 1$ , while for limb-darkened emission we have  $\Upsilon = \frac{1}{2} + \frac{3}{4} \cos \xi$ .

The second part of the calculation of the thermal spectrum is related to the propagation of the radiation from the disk to the observer. The image plane of the observer has Cartesian coordinates  $(X, Y)$ . The photons emitted from the disk and detected by the observer have 3-momentum perpendicular to the image plane. The photon trajectory can be integrated backwards in time from the image plane to the point of the emission on the accretion disk. In this way, one finds the radial coordinate  $r_e$  of the photon emission on the equatorial plane and the angle  $\xi$  between the wavevector of the photon and the normal of the disk surface. The image plane of the observer is divided into a number of small elements, and the ray-tracing procedure provides the observed flux density from each element. Integrating over all these elements, one finds the total observed flux density of the disk. The photon flux number density is

$$N_{E_{\text{obs}}} = \frac{1}{E_{\text{obs}}} \int I_{\text{obs}}(\nu) d\Omega_{\text{obs}} = \frac{1}{E_{\text{obs}}} \int g^3 I_e(\nu_e) d\Omega_{\text{obs}} = A_1 \left(\frac{E_{\text{obs}}}{\text{keV}}\right)^2 \int \frac{1}{M^2} \frac{\Upsilon dX dY}{\exp\left[\frac{A_2}{g^{F^{1/4}}} \left(\frac{E_{\text{obs}}}{\text{keV}}\right)\right] - 1}. \quad (4)$$

$E_{\text{obs}}$ ,  $I_{\text{obs}}$ , and  $\nu$  are, respectively, the photon energy, the specific intensity of the radiation, and the photon frequency measured by the distant observer.  $I_e(\nu_e)/\nu_e^3 = I_{\text{obs}}(\nu)/\nu^3$  is a consequence of the Liouville theorem.  $d\Omega_{\text{obs}} = dX dY/d^2$  is the element of the solid angle subtended by the image of the disk on the observer's sky,  $d$  is the distance of the source, and  $A_1$  and  $A_2$  are given by

$$A_1 = \frac{2(\text{keV})^2}{f_{\text{col}}^4} \left(\frac{G_N M}{c^3 h d}\right)^2 = \frac{0.07205}{f_{\text{col}}^4} \left(\frac{M}{M_\odot}\right)^2 \left(\frac{\text{kpc}}{d}\right)^2 \gamma \text{keV}^{-1} \text{cm}^{-2} \text{s}^{-1},$$

$$A_2 = \left(\frac{\text{keV}}{k_B f_{\text{col}}}\right) \left(\frac{G_N M}{c^3}\right)^{1/2} \left(\frac{4\pi\sigma}{\dot{M}}\right)^{1/4} = \frac{0.1331}{f_{\text{col}}} \left(\frac{10^{18} \text{g s}^{-1}}{\dot{M}}\right)^{1/4} \left(\frac{M}{M_\odot}\right)^{1/2}. \quad (5)$$

$g$  is the redshift factor

$$g = \frac{\nu}{\nu_e} = \frac{k_\mu u_o^\mu}{k_\mu u_e^\mu}, \quad (6)$$

where  $u_o^\mu = (1, 0, 0, 0)$  is the 4-velocity of the observer and  $u_e^\mu = (u_e^t, 0, 0, \Omega u_e^t)$  is the 4-velocity of the emitter. From the normalization condition  $g_{\mu\nu} u_e^\mu u_e^\nu = -1$ , one finds  $u_e^t$  as a function of  $r_e$

$$u_e^t = \frac{1}{\sqrt{-g_{tt} - 2g_{t\phi}\Omega - g_{\phi\phi}\Omega^2}}. \quad (7)$$

Since the spacetime is stationary and axisymmetric,  $k_\phi/k_t = \lambda$  is a constant along the photon path and it can be calculated from the photon initial conditions on the image plane of the observer, where the spacetime can be assumed flat. One eventually finds the redshift factor as a function of  $X$  and  $Y$

$$g = \frac{\sqrt{-g_{tt} - 2g_{t\phi}\Omega - g_{\phi\phi}\Omega^2}}{1 + \lambda\Omega}. \quad (8)$$

The relativistic effects of Doppler boost and gravitational redshift are entirely encoded in  $g$ . The ray-tracing calculation adds the effect of light bending.

### 3. TESTING THE NATURE OF BLACK HOLE CANDIDATES

The formalism reviewed in the previous section is very general, in the sense that it can be applied for any stationary, axisymmetric, and asymptotically flat spacetime. In the special case of the Kerr background, the ray-tracing part of the calculation of the photon trajectories from the disk to the observer's image plane can be significantly simplified, because the spacetime is of Petrov type D and in Boyer-Lindquist coordinates the photon equations of motion are separable and of first order. This is not true in the general case, and our code solves the second order photon geodesic equations. As background geometry, here we adopt the Johannsen-Psaltis metric. In Boyer-Lindquist coordinates, the line element is (Johannsen & Psaltis 2011b)

$$ds^2 = - \left(1 - \frac{2Mr}{\Sigma}\right) (1+h) dt^2 - \frac{4aMr \sin^2 \theta}{\Sigma} (1+h) dt d\phi + \frac{\Sigma(1+h)}{\Delta + a^2 h \sin^2 \theta} dr^2 + \Sigma d\theta^2 + \left[ \sin^2 \theta \left( r^2 + a^2 + \frac{2a^2 Mr \sin^2 \theta}{\Sigma} \right) + \frac{a^2 (\Sigma + 2Mr) \sin^4 \theta}{\Sigma} h \right] d\phi^2, \quad (9)$$

where

$$\begin{aligned} \Sigma &= r^2 + a^2 \cos^2 \theta, \\ \Delta &= r^2 - 2Mr + a^2, \\ h &= \sum_{k=0}^{\infty} \left( \epsilon_{2k} + \frac{Mr}{\Sigma} \epsilon_{2k+1} \right) \left( \frac{M^2}{\Sigma} \right)^k. \end{aligned} \quad (10)$$

The Johannsen-Psaltis metric has an infinite number of deformation parameters  $\epsilon_i$  and it includes the Kerr solution as the special case in which all the deformation parameters vanish. The correct Newtonian limit is recovered for  $\epsilon_0 = 0$ . Solar System experiments require  $\epsilon_1, \epsilon_2 \ll 1$  (assuming the validity of the Birkhoff theorem) (Cardoso et al. 2014). In the rest of this paper, we restrict our attention to the deformation parameter  $\epsilon_3$  and we set to zero all the others. All the deformation parameters have a similar impact on the geometry of the spacetime (Bambi 2012a). For  $\epsilon_i > 0$ , the BH is more oblate than its Kerr counterpart with the same spin and the gravitational force on the equatorial plane is weaker. For  $\epsilon_i < 0$ , the BH is more prolate than the Kerr one and the gravitational force on the equatorial plane is stronger. Here, we consider a single deformation parameter because this is the simplest case. While this choice cannot address generic deviations from the Kerr solution, with current observations it is already difficult to get an estimate of one deformation parameter.

With the metric in Eq. (9), we can compute the expected thermal spectrum of thin accretion disks and compare the predictions with observational data. The result is a constraint on the spin parameter–deformation parameter plane. Let us note that, strictly speaking, this approach can only test the Kerr geometry around a BH candidate and does not test the validity of the Einstein equations. Indeed, while the Kerr metric is the only vacuum BH solution in 4-dimensional general relativity, it is a solution even in other theories of gravity (Psaltis et al. 2008). The thermal spectrum of a thin disk is determined by the geodesic motion of the gas in the disk and of the photons from the disk to the observer. Our approach cannot distinguish a Kerr BH of general relativity from a Kerr BH in another theory of gravity because the geodesic equations are the same in the two scenarios.

Tab. 1 shows the spin measurements from the continuum-fitting method reported in the literature and obtained assuming the Kerr nature of BH candidates. The first column reports the name of the binary system, the second column shows the mass measurement of the BH candidates, the third column is for the estimate of the inclination angle of the disk, the forth column reports the spin measurement, and the fifth column is for the reference of the spin measurement. The BH mass  $M$  and the inclination angle of the disk  $i$  are usually inferred with dynamical models and optical observations, as they are input parameters in the continuum-fitting approach. In some cases, the angle  $i$  is estimated from the orientation of the BH jet, assuming that it is parallel to the BH spin and perpendicular to the accretion disk. See the original papers for more details and McClintock et al. (2011, 2013) for a general discussion. In what follows, we only consider the first 10 BH candidates in this table, while we neglect the last 3. The constraint on the spin parameter of the BH candidate in GX 339-4 is very weak and it could only rule out half part of the spin parameter–deformation parameter plane. The two recent studies of GS 1124-683 and of the microquasar in M31 seem to indicate that the accretion disk of these objects is counterrotating, but in this case the applicability of the continuum-fitting method is more questionable. So we prefer to focus our attention only on those measurements that are supposed to be the most robust and reliable.

BH Binary	$M/M_\odot$	$i$	$a_*$	Reference
GRO J1655-40	$6.30 \pm 0.27$	$70.2^\circ \pm 1.2^\circ$	$0.70 \pm 0.10$	Shafee et al. (2006)
4U 1543-47	$9.4 \pm 1.0$	$20.7^\circ \pm 1.5^\circ$	$0.80 \pm 0.10$	Shafee et al. (2006)
GRS 1915+105	$14.0 \pm 4.4$	$66^\circ \pm 2^\circ$	$> 0.98$	McClintock et al. (2006)
M33 X-7	$15.65 \pm 1.45$	$74.6^\circ \pm 1.0^\circ$	$0.84 \pm 0.05$	Liu et al. (2008, 2010)
LMC X-1	$10.91 \pm 1.54$	$36.38^\circ \pm 2.02^\circ$	$0.92^{+0.05}_{-0.07}$	Gou et al. (2009)
A0620-00	$6.61 \pm 0.25$	$51.0^\circ \pm 0.9^\circ$	$0.12 \pm 0.19$	Gou et al. (2010)
XTE J1550-564	$9.10 \pm 0.61$	$74.7^\circ \pm 3.8^\circ$	$0.34^{+0.20}_{-0.28}$	Steiner et al. (2011)
Cygnus X-1	$14.8 \pm 1.0$	$27.1^\circ \pm 0.8^\circ$	$> 0.98$	Gou et al. (2011, 2014)
H1743-322	$\sim 10$	$75^\circ \pm 3^\circ$	$0.2 \pm 0.3$	Steiner et al. (2012)
LMC X-3	$6.95 \pm 0.33$	$69.6^\circ \pm 0.6^\circ$	$0.21 \pm 0.12$	Steiner et al. (2014)
GX 339-4	$5.8 - 15$	$20^\circ - 70^\circ$	$< 0.9$	Kolehmainen & Done (2010)
GS 1124-683	$7.24 \pm 0.70$	$54^\circ \pm 1.5^\circ$	$< -0.2$	Morningstar et al. (2014)
M31 microquasar	$\sim 10$	$\sim 32^\circ, \sim 39^\circ$	$< -0.2$	Middleton et al. (2014)

TABLE 1

CONTINUUM-FITTING MEASUREMENTS OF THE SPIN PARAMETER OF STELLAR-MASS BH CANDIDATES REPORTED IN THE LITERATURE UNDER THE ASSUMPTION OF THE KERR BACKGROUND. SEE THE REFERENCES IN THE LAST COLUMN FOR MORE DETAILS.

In our non-Kerr model, the thermal spectrum of thin disks depends on 3 free parameters, namely  $a_*$ ,  $\epsilon_3$ , and  $\dot{M}$ , because with the continuum-fitting method  $M$ ,  $d$ , and  $i$  are to be determined by independent measurements. One can thus compute a number of spectra and fit the data to infer  $a_*$ ,  $\epsilon_3$ , and  $\dot{M}$ . In this paper, we use instead an approach that exploits the fundamental degeneracy between  $a_*$  and  $\epsilon_3$ . While the procedure significantly simplify the analysis, we argue (see below) that the final result is very similar, especially in the cases of slow-rotating objects, which show a true degeneracy between  $a_*$  and  $\epsilon_3$ . We replace the observational data with the theoretical spectrum of a Kerr BH with spin parameter given by the measurement shown in Tab. 1. We compute the  $\chi^2$  by comparing this reference spectrum with the one of a Johannsen-Psaltis BH with spin parameter  $a_*$ , deformation parameter  $\epsilon_3$ , and mass accretion rate  $\dot{M}$ :

$$\chi^2(a_*, \epsilon_3, \dot{M}) = \sum_{i=1}^n \frac{[N_i(a_*, \epsilon_3, \dot{M}) - N'_i(a'_*, \epsilon'_3, \dot{M}')]^2}{\sigma_i^2}, \quad (11)$$

where the summation is performed over  $n$  sampling energies  $E_i$ ,  $N_i$  and  $N'_i$  are, respectively, the photon fluxes in the energy bin  $[E_i, E_i + \Delta E]$  for the non-Kerr model and the reference Kerr model.  $a'_*$ ,  $\epsilon'_3 = 0$ , and  $\dot{M}'$  are the spin parameter, the vanishing deformation parameter, and the mass accretion rate of the reference Kerr model. The error  $\sigma_i$  is assumed to be proportional to the mean value of  $N_i$  and  $N'_i$ , but our results will be independent of the constant of proportionality. This is a simple method to quantify the level of correspondence between the spectra of the two models (Jiang et al. 2014). We note that we should have assumed  $\sigma_i$  proportional to the square root of the mean value of  $N_i$  and  $N'_i$  if either a measurement was obtained using some sort of photon counting instrument or we are making predictions about what a hypothetical detector's error would be. Here we are comparing the correspondence of two models in model-space; that is, something which has nothing to do with a physical detector and it makes sense to assume that the error is proportional to the mean value of  $N_i$  and  $N'_i$ .

The mass  $M$  and the distance  $d$  only alter the normalization of the photon flux; here we use the same values in the two models (we basically assume that the dynamical measurements are correct) and they do not have any effect on our final constraints. The value of the inclination angle  $i$  is instead important, because it has an impact on the effect of light bending, and we use the measurements shown in the third column of Tab. 1 for any object. Concerning the mass accretion rate, within the continuum-fitting method it is an output parameter to be inferred during the fitting procedure. We cannot use the mass accretion rate found in the measurements reported in the literature, because its estimate is correlated to the one of the spin parameter [see Fig. 4a in Gou et al. (2009)]. The measurement of the accretion luminosity  $L_{\text{acc}} = \eta \dot{M}$ , where  $\eta$  is the radiative efficiency, is instead not correlated to the measurement of  $a_*$  [see Fig. 4b in Gou et al. (2009)]. In our analysis we thus use a constant accretion luminosity and  $\dot{M}$  is given by:

$$\dot{M} = \frac{\eta' \dot{M}'}{\eta}, \quad (12)$$

where  $\eta = \eta(a_*, \epsilon_3)$  and  $\eta'$  are, respectively, the radiative efficiency in the non-Kerr and reference Kerr models, namely  $\eta = 1 - E_{\text{ISCO}}(a_*, \epsilon_3)$  and  $\eta' = 1 - E_{\text{ISCO}}(a'_*)$ , where  $E_{\text{ISCO}}$  is the specific energy at the ISCO radius and depends on the background metric. The exact value of the accretion luminosity does not affect the final results, so the important point is that we impose that  $\dot{M}$  scales as the inverse of  $\eta$ .

For any value of  $\epsilon_3$ ,  $\chi^2$  has one or more local minima, which can be indicated by  $\chi^2_{\text{min}}(\epsilon_3)$ . For  $\epsilon_3 = 0$ , the minimum of  $\chi^2$  is exactly zero, by definition, but it is usually very close to zero even for a non-vanishing  $\epsilon_3$ . Let us call  $\sigma_-$  and  $\sigma_+$  the values of  $\chi^2$  for  $\epsilon_3 = 0$  corresponding, respectively, to the 1-sigma lower and upper measurements of the BH spin parameter in Tab. 1. We can then define two kinds of constraints on the spin parameter–deformation parameter plane. If BH candidates are really Kerr BHs, the analysis of real data would be able to rule out all the



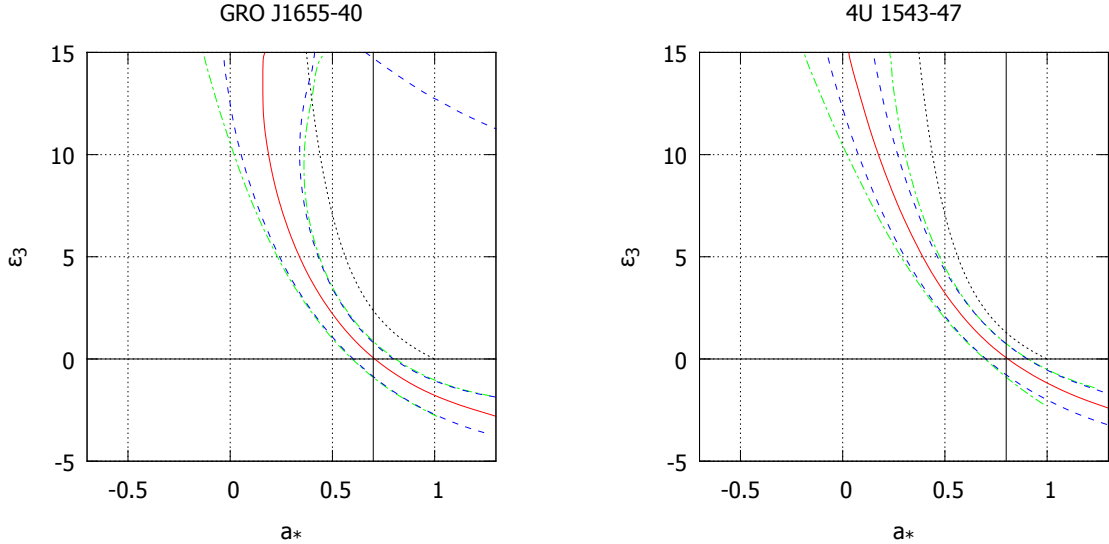


FIG. 1.— Disk’s thermal spectrum constraints on possible deviations from the Kerr geometry in the spacetime around the BH candidates in GRO J1655-40 (left panel) and 4U 1543-47 (right panel). Here and in the other plots of this paper, the red-solid curve is  $\chi^2_{\min}(\epsilon_3)$ , the blue-dashed curves are  $\sigma_-$  and  $\sigma_+$ , respectively on the left and right side of the red-solid line, while the green-dashed-dotted curves are  $\chi^2_{\min}(\epsilon_3) + \sigma_-$  and  $\chi^2_{\min}(\epsilon_3) + \sigma_+$ , respectively on the left and right side of the red-solid line. See the text for more details.

models with  $\chi^2 > \sigma_-$  on the left of  $\chi^2_{\min}(\epsilon_3)$  and all the models with  $\chi^2 > \sigma_+$  on the right of  $\chi^2_{\min}(\epsilon_3)$ . As already noted, in this way it is not important the constant of proportionality between  $\sigma_i$  and the mean value of  $N_i$  and  $N'_i$ . The second type of constraint is obtained by considering the region with  $\chi^2 < \chi^2_{\min}(\epsilon_3) + \sigma_-$  on the left of  $\chi^2_{\min}(\epsilon_3)$  and the region with  $\chi^2 < \chi^2_{\min}(\epsilon_3) + \sigma_+$  on the right of  $\chi^2_{\min}(\epsilon_3)$ . In presence of a perfect degeneracy between the  $a_*$  and  $\epsilon_3$ , the two kinds of constraints would be equivalent, as  $\chi^2_{\min}(\epsilon_3)$  should vanish. This is indeed what happens for slow-rotating objects within a good approximation. However, within our framework of the Johannsen-Psaltis metric with deformation parameter  $\epsilon_3$ , such a degeneracy may not be realized for fast-rotating objects and high values of  $\epsilon_3$ . In this case, it would make sense to consider the second type of constraint region, but actually one should be able to see it within a Kerr model, finding that the minimum of  $\chi^2$  is much larger than the expected one. Within a Kerr model, this would be interpreted as a sign of over-fitting, over-confidence, or some other analysis error. In what follows, we show both the constraints: the second one can at least be used as a guide to figure out when  $\chi^2_{\min}(\epsilon_3)$  is close to zero and when it is not.

#### 4. RESULTS

Figs. 1-4 show the constraints for the 10 stellar-mass BH candidates obtained with the procedure discussed in Section 3. We note that a large region of the spin parameter–deformation parameter plane describes spacetimes with naked singularities [see Fig. 2 in Johannsen & Psaltis (2011b)]. In all our figures, the black dotted line starting from  $a_* = 1$  and  $\epsilon_3 = 0$  and moving to lower  $a_*$  for  $\epsilon_3 > 0$  is the boundary separating spacetime with and without naked singularities. Spacetimes with naked singularities are on the right side of the black dotted line and in the Kerr limit  $\epsilon_3 = 0$  we recover the well known fact that a naked singularity is present for  $a_* > 1$ . For  $\epsilon_3 < 0$ , the BH horizon looks like a doughnut with a singularity at the center for  $a_* > 1$  (Bambi & Modesto 2011). Here we have not automatically excluded such a region, because the continuum-fitting method can only test the spacetime geometry at radii larger than the ISCO and we have no information on the spacetime at smaller radii. For instance, the metric in Eq. (9) may be the exterior solution of an exotic object and be valid up to the radius of its surface, while at smaller radii we could have an interior solution without singularities. We also note that in some plots the contours of  $\chi^2$  end at some point. This is either because we are at the boundary of our plane and there are not enough calculated spectra, or because there are peculiar features that make the constraint ambiguous (for instance, the green-dashed-dotted line in presence of two different local minima for a fixed  $\epsilon_3$ ). In any case, this only happens for a few cases and large deviations from Kerr, so it is not a problem for the future applications of these constraints that we have in mind.

Concerning the reliability of the bounds found with this approach, we note that the thermal spectrum of thin disks has a very simple shape (Bambi 2013b). In most cases, there is a true degeneracy between  $a_*$  and  $\epsilon_3$ . We thus believe that there is not the danger of erroneously weighting different portion of the spectrum, just because the same result should be generally found from the analysis of every part. From this point of view, the only BH candidate that might benefit of a complete data reanalysis is the object in LMC X-1, for which at high values of  $\epsilon_3$  there is a departure from the spectrum obtained in the Kerr background. The approach used here would provide instead more suspicious results in the case of the study of features with a more complicated structure, e.g. the iron  $K\alpha$  line, because in that case different relativistic effects show up in different parts of the spectrum and thus it is important to compare different

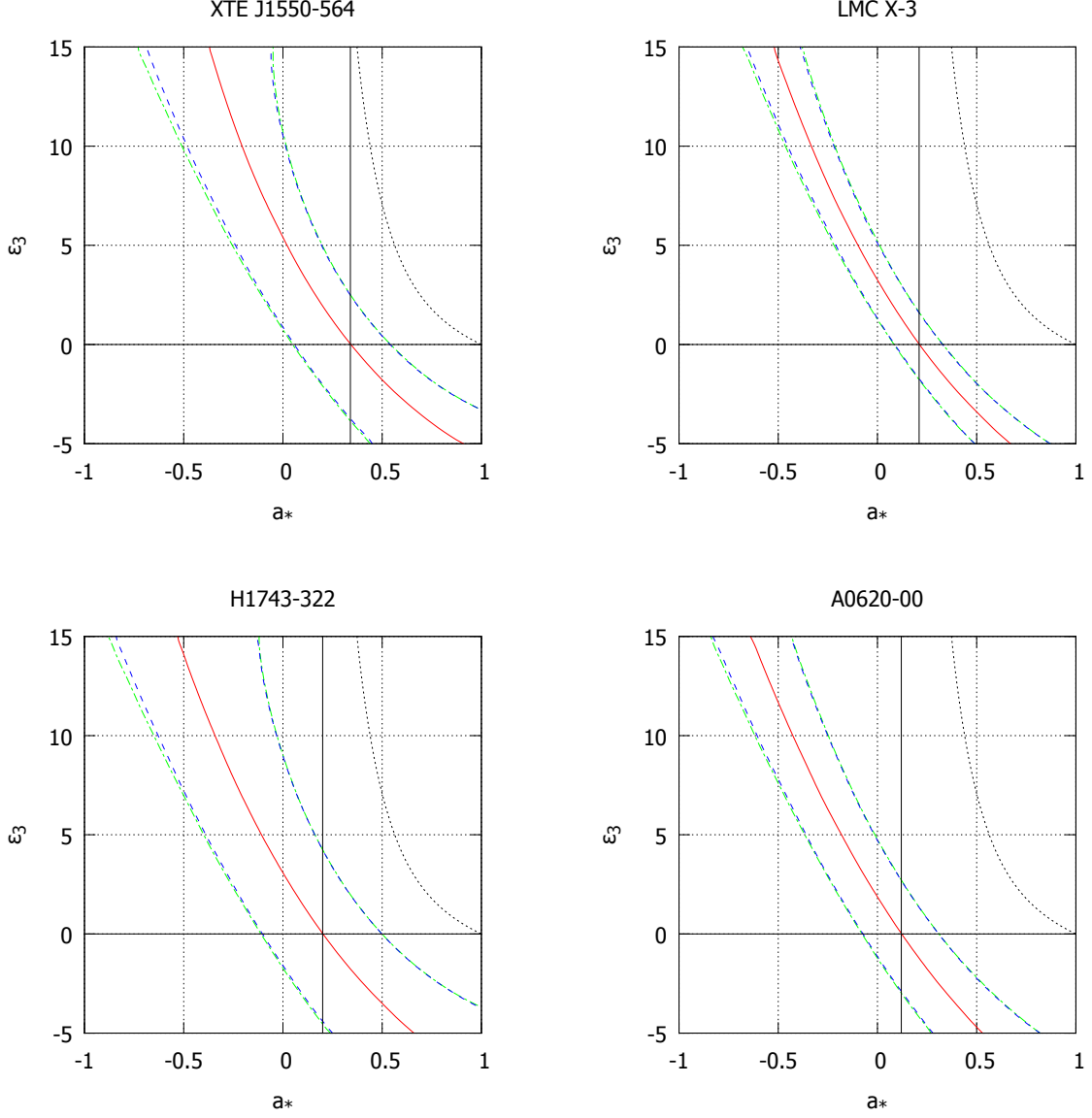


FIG. 2.— As in Fig. 1 for the BH candidates in XTE J1550-564 (top left panel), LMC X-3 (top right panel), H1743-322 (bottom left panel), and A0620-00 (bottom right panel). See the text for more details.

parts of the spectrum with their actual uncertainty.

#### 4.1. *GRS J1655-40 and 4U 1543-47*

GRS J1655-40 and 4U 1543-47 were the first two sources for which the continuum-fitting method was applied to estimate the spin parameters of BH candidates (Shafee et al. 2006) [previous attempts in Zhang et al. (1997) were only to illustrate the procedure, but serious measurements were not possible because of the poor quality of the data and of systematic effects not fully under control]. Our constraints on the spin parameter–deformation parameter plane are reported in Fig. 1. The red-solid lines track the local minima of  $\chi^2$ ,  $\chi^2_{\min}(\epsilon_3)$ . The blue-dashed lines are for  $\sigma_-$  and  $\sigma_+$ , respectively, to the 1-sigma lower and upper measurements of the BH spin parameter in Tab. 1. For instance, in the case of GRO J1655-40,  $\sigma_- = \chi^2(a_* = 0.6, \epsilon_3 = 0)$  and  $\sigma_+ = \chi^2(a_* = 0.8, \epsilon_3 = 0)$ . The regions on the left side of the red-solid lines and between the red-solid lines and the blue-dashed lines include BHs with  $0 < \chi^2 < \sigma_-$ . The regions on the right hand side of the red-solid lines and between the red-solid lines and the blue-dashed lines are for BHs with  $0 < \chi^2 < \sigma_+$ . Objects with  $a_*$  and  $\epsilon_3$  between the two blue-dashed lines are indistinguishable from a Kerr BH with the reference spin within the current uncertainties. The green-dashed-dotted lines are instead for  $\chi^2_{\min}(\epsilon_3) + \sigma_-$  and  $\chi^2_{\min}(\epsilon_3) + \sigma_+$ , respectively on the left and right sides of the red-solid lines. Both for GRS J1655-40 and 4U 1543-47 the difference between the two kinds of constraints is small.

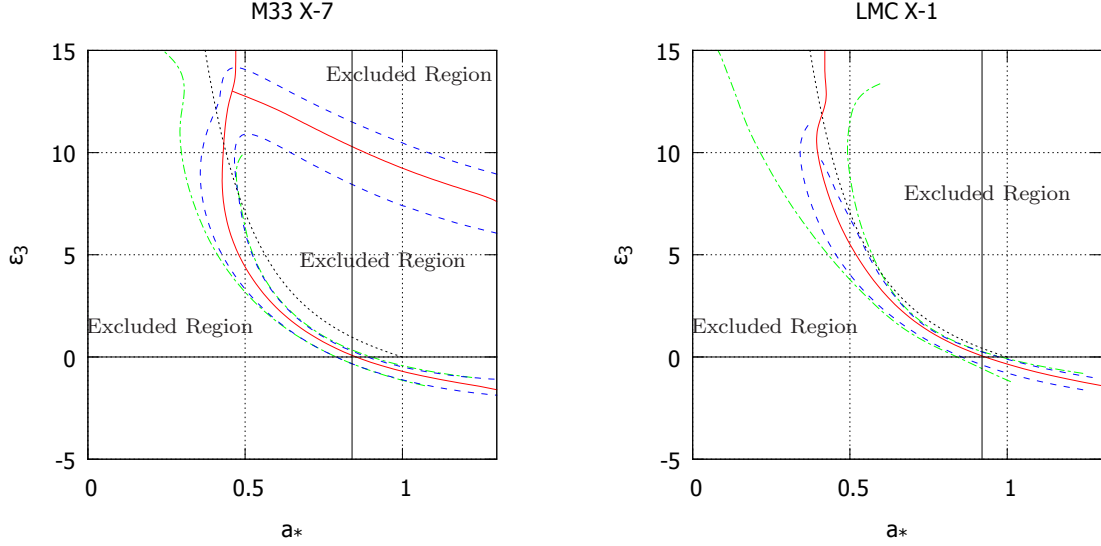


FIG. 3.— As in Fig. 1 for the BH candidates in M33 X-7 (left panel) and LMC X-1 (right panel). See the text for more details.

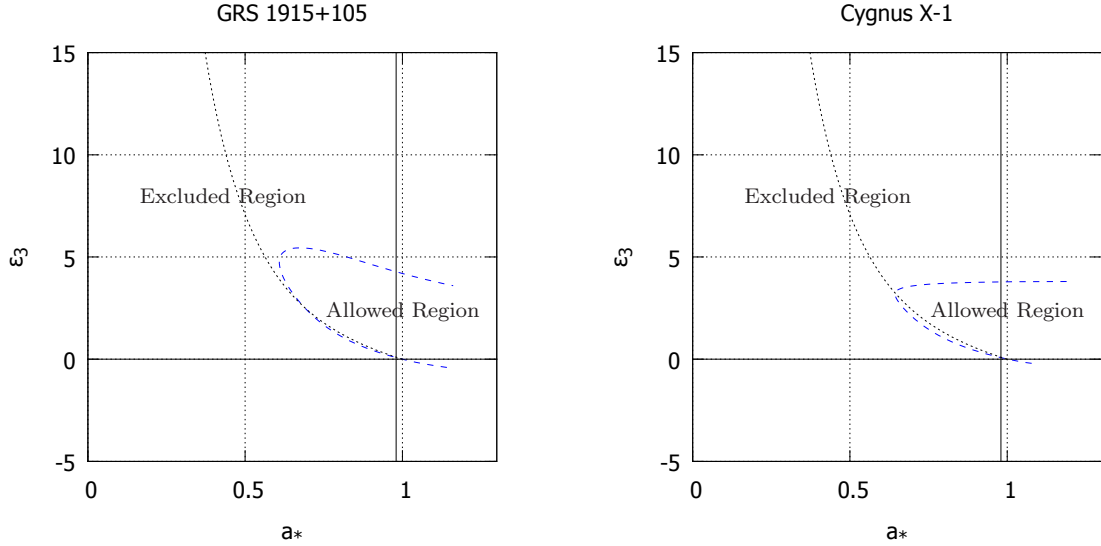


FIG. 4.— As in Fig. 1 for the BH candidates in GRS 1915+105 (left panel) and Cygnus X-1 (right panel). See the text for more details.

While the constraints on the spin parameter–deformation parameter plane primarily depend on the measurement of the spin in the Kerr background, a minor role is played by the value of the disk’s inclination angle with respect to our line of sight. The effect of  $i$  becomes more pronounced for  $\epsilon_3 > 10$ : for high values of  $\epsilon_3$ , the preferred spin parameter  $a_*$  is larger for higher  $i$  than the one that would be obtained for lower  $i$ . To make more clear this statement, in the top panel of Fig. 5 we show the continuum-fitting method constraints that would have been obtained for GRO J1655-40 assuming an inclination angle  $i = 20^\circ$  instead of  $i = 70.2^\circ$ . At  $\epsilon_3 = 15$ , the spin measurement for  $i = 20^\circ$  is  $a_* = -0.13^{+0.10}_{-0.18}$ , while for  $i = 70.2^\circ$  one finds  $a_* = 0.17 \pm 0.30$ . For instance, the inclination angle is the key-point for the difference between the shape of the constraints for GRO J1655-40 and 4U 1543-47 in Fig. 1. In the Kerr background, one finds respectively  $a_* = 0.7 \pm 0.1$  and  $a_* = 0.8 \pm 0.1$ ; that is, 4U 1543-47 rotates faster than GRO J1655-40. For high values of the deformation parameter, one finds instead that GRO J1655-40 would rotate faster than 4U 1543-47.

Concerning the choice of the mass accretion rate, here we are assuming the same accretion luminosity  $L_{\text{acc}} = \eta \dot{M}$  in all the models. As shown in Gou et al. (2009), the estimate of  $a_*$  and  $\dot{M}$  in the Kerr background are correlated, and therefore in our analysis we cannot assume a constant mass accretion rate. On the contrary, the estimate of the



accretion luminosity is not correlated with the measurement of  $a_*$ . In Fig. 5, we show the constraints that would have been obtained for GRO J1655-40 in the case of  $\dot{M} = \dot{M}'$ , respectively for an inclination angle  $i = 70.2^\circ$  (bottom left panel) and  $20^\circ$  (bottom right panel). In the case of a low inclination angle,  $i = 20^\circ$ , one finds more or less the same constraints, see the top panel and the bottom right panel in Fig. 5. For  $i = 70.2^\circ$ , the difference is larger, but only for  $\epsilon_3 > 10$ .

Lastly, let us note that in previous work on tests of the Kerr nature of BH candidates we have used as crude approximation of the continuum-fitting measurements the values of the Novikov-Thorne radiative efficiency  $\eta = 1 - E_{\text{ISCO}}$  (Bambi 2012b,c,d); that is, at first approximation the continuum-fitting method actually measures the radiative efficiency in the Novikov-Thorne model. We thus exploited this fact translating the spin measurements in the Kerr background into radiative efficiency measurements, and then the latter into spin measurements for Johannsen-Psaltis BHs with non-vanishing deformation parameter  $\epsilon_3$ . In the left panel of Fig. 6, we show the constraints that can be obtained with this approximation for the BH candidate in GRO J1655-40. In the Kerr background, the spin measurement is  $a_* = 0.7$  and the 1-sigma lower and upper bounds are, respectively,  $a_* = 0.6$  and  $0.8$ . These three values of the spin parameter correspond to  $\eta = 0.1036, 0.0912$ , and  $0.1221$  in the Kerr metric. In the left panel in Fig. 6, the red-solid line marks the objects with Novikov-Thorne radiative efficiency  $\eta = 0.1036$ , while the blue-dashed lines are for spacetimes with  $\eta = 0.0912$  and  $0.1221$ . The constraints obtained with this simplification (that clearly does not take the inclination angle into account) seem to provide a quite good result if the inclination angle of the disk is low, while there is a more significant departure from the correct measurement in the case of high inclination angles. For instance, for  $\epsilon_3 = 15$  one finds  $a_* = -0.09 \pm 0.15$  from the  $\eta$ -approach, to be compared with the spin measurement  $a_* = -0.13^{+0.10}_{-0.18}$  for the case  $i = 20^\circ$  and the estimate  $a_* = 0.17 \pm 0.30$  for  $i = 70.2^\circ$ . In the right panel in Fig. 6, we show the contour levels for a Keplerian frequency at the ISCO radius  $\Omega_{\text{ISCO}}/M = 0.1439$  (red-solid lines) and  $0.1236$  and  $0.1737$  (blue-dashed lines). In the case of Kerr background, these values correspond to spacetimes with  $a_* = 0.7, 0.6$  and  $0.8$ , so the case of GRO J1655-40. The radiative efficiency is a better proxy for the continuum-fitting measurements.

#### 4.2. Slow-rotating objects: XTE J1550-564, LMC X-3, H1743-322, and A0620-00

Fig. 2 shows the constraints for XTE J1550-564 (top left panel), LMC X-3 (top right panel), H1743-322 (bottom left panel), and A0620-00 (bottom right panel). Even if the measurement of  $a_*$  depends on the value of  $\epsilon_3$ , in any case all these objects can be classified as slow-rotating. Here  $\chi^2_{\text{min}}(\epsilon_3)$  is always very close to zero and the difference between the constraints given by the blue-dashed curves and the green-dashed-dotted curves is definitively small. For these objects, there is a true degeneracy between  $a_*$  and  $\epsilon_3$ , which is the best situation to employ our approach.

#### 4.3. Fast-rotating objects: M33 X-7 and LMC X-1

Fig. 3 reports the constraints for the BH candidates in M33 X-7 (left panel) and LMC X-1 (right panel). These objects can be roughly classified as fast-rotating and their constraints present some new features for large values of the deformation parameter. For small values of  $\epsilon_3$ , say  $\epsilon_3 \lesssim 10$  for M33 X-7 and  $\epsilon_3 \lesssim 5$  for LMC X-1,  $\chi^2_{\text{min}}(\epsilon_3)$  is still close to zero and the difference between the constraints provided by the blue-dashed and green-dashed-dotted curves is small. For larger values of  $\epsilon_3$ ,  $\chi^2_{\text{min}}(\epsilon_3)$  can significantly differ from zero, the bounds provided by the blue-dashed and green-dashed-dotted curves tend to disagree, and actually it is possible to get a bound on  $\epsilon_3$ . These constraints can be understood in terms of the location of the ISCO radius or, more precisely, in terms of the radiative efficiency in the Novikov-Thorne model, namely  $\eta = 1 - E_{\text{ISCO}}$ . The radial coordinate of the ISCO radius has indeed no physical meaning in general relativity, being the choice of the coordinate system arbitrary. The continuum-fitting method eventually measure something similar to  $\eta$  and, as shown in Fig. 7, the radiative efficiency can be very high only for small values  $|\epsilon_3|$ . This explains the two local minima of  $\chi^2$  found in the plot of M33 X-7 for  $7 < \epsilon_3 < 13$  in the range of our plane. The actual constrain for this object is given by the region between the two blue-dashed curves. Roughly speaking, the disk thermal spectrum of the BHs inside the internal blue-dashed line looks more like the one of Kerr BHs with spin parameter larger than the upper bound inferred assuming the Kerr background, namely  $a_* = 0.89$ . The spectrum of the BHs outside the external blue-dashed line is more similar to the one of Kerr BHs with spin parameter lower than the lower bound inferred assuming the Kerr metric,  $a_* = 0.79$ . If we assume the Kerr background and we analyze the X-ray data of the thermal spectrum of a thin disk in a Johannsen-Psaltis background located outside the exterior blue-dashed curve, we would obtain a lower spin parameter than the one measured. The 1-sigma bound  $a_* > 0.79$  obtained in the Kerr background thus implies a spin independent constraint  $\epsilon_3 < 14$ . While the red-solid line for  $\epsilon_3 > 14$  above the connection point is still the minimum of  $\chi^2$ , the spectrum of these objects are more similar to the ones of Kerr BH with spin  $a_* < 0.79$ .

The constraints for LMC X-1 are actually similar, even if they look to be very different at a first sight. The difference in the allowed regions of M33 X-7 and LMC X-1 is due to the different inclination angle (high  $i$  for M33 X-7, low  $i$  for LMC X-1), the higher value of the spin parameter inferred for LMC X-1, and the precision of the Kerr measurement. Because of the lower inclination angle, LMC X-1 has not two local minima of  $\chi^2$  in the range under consideration (we would have found the second minimum, as well as the connection point between the two minima, if we had included higher values of  $\epsilon_3$ ). Moreover, the blue-dashed curve closes at  $\epsilon_3 \approx 11$  because the spectra in spacetimes with higher deformation parameter have  $\chi^2$  larger than  $\sigma_-$  and  $\sigma_+$ <sup>1</sup>. If the Kerr spin measurement of LMC X-1 had a larger

<sup>1</sup> We note that the blue-dashed curve closes: it may not be clear from the picture simply because it overlaps with the red line.

uncertainty than the 1-sigma bound  $0.85 < a_* < 0.97$ , we would have obtained a larger allowed region on the spin parameter–deformation parameter plane, the blue-dashed curve would have not closed, and the constraint would have looked more similar to the one of M33 X-7. If, for instance, the BH candidate in LMC X-1 were a Johannsen-Psaltis BH with  $\epsilon_3 = 13$ , the analysis of the disk’s thermal spectrum under the assumption of Kerr background would provide the spin parameter reported in Tab. 1 for the objects on the red-solid line, but the fit would not be good. In the case of LMC X-1, the analysis of real data may distinguish a Kerr BH from one with  $\epsilon_3 > 11.5$ .

#### 4.4. Very fast-rotating objects: GRS1915+105 and Cygnus X-1

For the BH candidates in GRS1915+105 and in Cygnus X-1, the Kerr spin measurement is just a lower bound,  $a_* > 0.98$ . The constraints on the spin parameter–deformation parameter plane are reported in Fig. 4 and they have been obtained following a slightly different approach, which is dictated by the fact that we have a lower bound instead of a measurement. The plots only show the blue-dashed lines, which here separate BHs whose spectrum looks more similar to the one of a Kerr BH with spin parameter higher/lower than 0.98. More precisely, the allowed regions are the ones inside the blue-dashed lines (the spectra of these BHs look like the one of a Kerr BH with spin parameter larger than 0.98), while the regions outside are ruled out (the spectra of these BHs would be interpreted as the one of a Kerr BH with spin lower than 0.98). The difference between the constraints of GRS1915+105 and Cygnus X-1 is only due to their different viewing angle. The remarkable difference with respect to the other BH candidate constraints is that here the deformation parameter  $\epsilon_3$  turns out to be well constrained. This happens because Johannsen-Psaltis BHs can mimic very fast-rotating Kerr BHs for a restricted range of the spin and the deformation parameters [but this is not true for other kinds of deformations, see Bambi (2014b)]. In the case of GRS1915+105, the Kerr bound  $a_* > 0.98$  implies  $\epsilon_3 < 6.0$ . For Cygnus X-1, the constraint is  $\epsilon_3 < 4.0$ . Again, these constraints could be expected on the basis of the radiative efficiency of the Johannsen-Psaltis spacetimes shown in Fig. 7<sup>2</sup>. We note, however, that the allowed regions for GRS1915+105 and Cygnus X-1 reported in Fig. 4 have also some very pathological spacetimes in which there is no ISCO and the radiative efficiency can be very high (potentially mimicking Kerr metrics with  $a_* > 1$ , but current measurements cannot rule out the possibility that these sources have a radiative efficiency exceeding the one of a Kerr BH with  $a_* = 1$ , see the original papers).

### 5. SUMMARY AND CONCLUSIONS

Astrophysical BH candidates are thought to be the Kerr BHs predicted in general relativity, but there is not yet an observational confirmation that the spacetime geometry around them is described by the Kerr solution. The observation of features associated to relativistic effects in their spectra is not enough to confirm the Kerr nature of these objects, because non-Kerr BHs may look like Kerr BHs with different spin (Bambi 2013d; Li & Bambi 2014; Li et al. 2014; Tsukamoto et al. 2014). To test the Kerr BH hypothesis, we have to consider a more general background that includes the Kerr solution as special case, and check whether observational data only require the Kerr solution.

The continuum-fitting methods is the analysis of the thermal spectrum of geometrically thin and optically thick accretion disks. Assuming that the spacetime around BH candidates is described by the Kerr metric, this technique is used to infer the BH spin parameter  $a_*$ . In the present paper, we have “translated” the spin measurements reported in the literature into constraints on the spin parameter–deformation parameter plane. This has been achieved by comparing Kerr models with the spin parameters reported in the literature with the spectra computed in the Johannsen-Psaltis metric. The approach is possible thanks to a fundamental degeneracy between the spin and possible deviations from the Kerr solution. This significantly simplifies the analysis, since we can just focus our attention on the role of the spacetime metric, assuming that all the astrophysical effects and the instrumental issues have been already properly taken into account in the previous studies.

The results of this work are Figs. 1-4. The constraints obtained here will be combined with other measurements to break the degeneracy between the spin parameter and the deformation parameter. The iron line profile is currently the only other relatively robust technique to probe the spacetime geometry around BH candidates and it has been already extended to non-Kerr backgrounds (Johannsen & Psaltis 2013; Bambi 2013a). However, only for a few sources we have good X-ray data for both the continuum-fitting method and the iron line profile. It is also to be noted that both the techniques strongly rely on the fact that the inner edge of the disk is at the ISCO radius, so their combination may not be the best choice to break the degeneracy and only very good measurement – not available today – could put interesting constraints (Bambi 2013d). A more promising approach could be the combination of the continuum-fitting constraints with current bounds from quasi-periodic oscillations (or QPO) (Johannsen & Psaltis 2011a; Bambi 2012d, 2013e), but at present it is not clear the exact mechanism responsible for these phenomena and different models predict different measurements, which makes this technique not yet mature to test fundamental physics.

We thank Lijun Gou and Jack Steiner for useful discussions and suggestions. This work was supported by the NSFC grant No. 11305038, the Shanghai Municipal Education Commission grant for Innovative Programs No. 14ZZ001, the Thousand Young Talents Program, and Fudan University.

<sup>2</sup> For high values of  $a_*$  and  $\eta$ , there is some discrepancy at the quantitative level between the constraints imposed by the two parameters. For instance, the Kerr spin estimate  $a_* > 0.98$  would require  $\eta > 0.234$ , while from the comparison of Fig. 4 and Fig. 7 it seems that the measurement  $a_* > 0.98$  is more similar to a bound such as  $\eta > 0.30$ . The constraints would have been very similar in the case we had imposed  $\dot{M} = \text{constant}$ , as it can be seen from the comparison of the right panel in Fig. 4 in Bambi (2013b) (where  $\dot{M} = \text{constant}$ ) and Fig. 7 in the present paper. Here the analysis has been conducted assuming  $\eta\dot{M} = \text{constant}$  for the reasons discussed in Section 3.

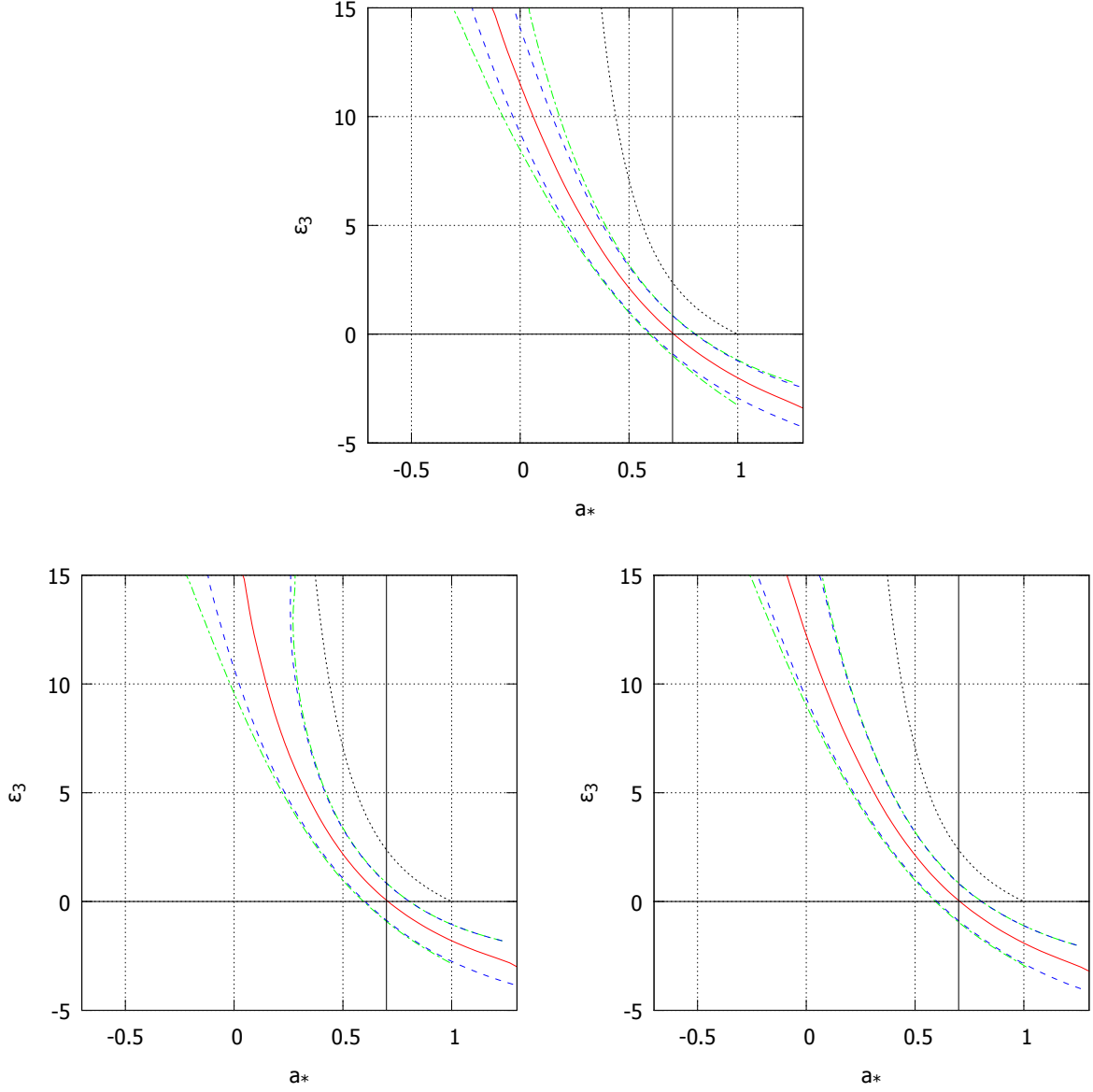


FIG. 5.— Top panel: Disk’s thermal spectrum constraints on possible deviations from the Kerr geometry in the spacetime around the BH candidate in GRO J1655-40 that would have been obtained with an inclination angle  $i = 20^\circ$ . Bottom panels: as in the top panel, using a constant mass accretion rate  $\dot{M} = \dot{M}'$  instead of  $\dot{M} = \eta' \dot{M}' / \eta$  in Eq. (12) and an inclination angle  $i = 70.2^\circ$  (left panel) and  $20^\circ$  (right panel). See the text for more details.

#### REFERENCES

- Bambi, C. 2011, *Modern Physics Letters A*, 26, 2453  
 Bambi, C. 2012a, *Phys. Rev. D*, 85, 043001  
 Bambi, C. 2012b, *Phys. Rev. D*, 85, 043002  
 Bambi, C. 2012c, *Phys. Rev. D*, 86, 123013  
 Bambi, C. 2012d, *J. Cosmol. Astropart. Phys.*, 9, 14  
 Bambi, C. 2012e, *ApJ*, 761, 174  
 Bambi, C. 2013a, *Phys. Rev. D*, 87, 023007  
 Bambi, C. 2013b, *The Astronomical Review*, 8, 4  
 Bambi, C. 2013c, *Phys. Rev. D*, 87, 084039  
 Bambi, C. 2013d, *J. Cosmol. Astropart. Phys.*, 8, 55  
 Bambi, C. 2013e, *arXiv:1312.2228*  
 Bambi, C. 2014a, *Physics Letters B*, 730, 59  
 Bambi, C. 2014b, *Phys. Rev. D*, 90, 047503  
 Bambi, C. 2014c, *arXiv:1409.0310*  
 Bambi, C., & Barausse, E. 2011, *ApJ*, 731, 121  
 Bambi, C., & Malafarina, D. 2013, *Phys. Rev. D*, 88, 064022  
 Bambi, C., & Modesto, L. 2011, *Physics Letters B*, 706, 13  
 Barausse, E., Cardoso, V., & Khanna, G. 2010, *Physical Review Letters*, 105, 261102  
 Broderick, A. E., Loeb, A., & Narayan, R. 2009, *ApJ*, 701, 1357  
 Cardoso, V., Pani, P., & Rico, J. 2014, *Phys. Rev. D*, 89, 064007  
 Carter, B. 1971, *Physical Review Letters*, 26, 331  
 Chruściel, P. T., Costa, J. L., & Heusler, M. 2012, *Living Reviews in Relativity*, 15, 7  
 Dotti, G., Gleiser, R. J., Ranea-Sandoval, I. F., & Vucetich, H. 2008, *Classical and Quantum Gravity*, 25, 245012  
 Giacomazzo, B., Rezzolla, L., & Stergioulas, N. 2011, *Phys. Rev. D*, 84, 024022  
 Gou, L., McClintock, J. E., Liu, J., et al. 2009, *ApJ*, 701, 1076  
 Gou, L., McClintock, J. E., Reid, M. J., et al. 2011, *ApJ*, 742, 85  
 Gou, L., McClintock, J. E., Remillard, R. A., et al. 2014, *ApJ*, 790, 29  
 Gou, L., McClintock, J. E., Steiner, J. F., et al. 2010, *ApJ*, 718, L122

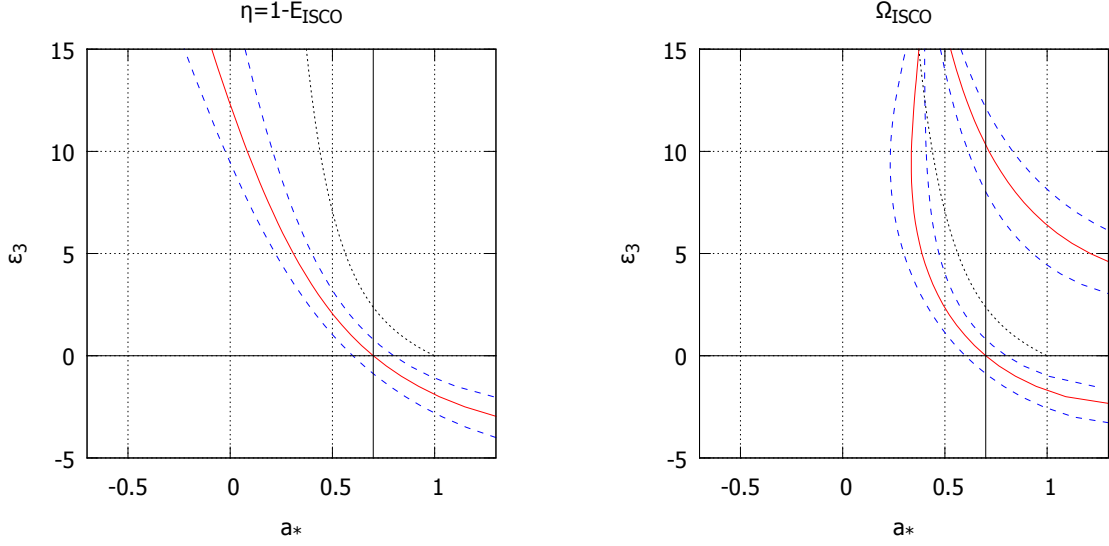


FIG. 6.— Left panel: radiative efficiency in the Novikov-Thorne model  $\eta = 1 - E_{\text{ISCO}}$ . The red-solid line is for  $\eta = 0.1036$ , which is the same as the one for a Kerr BH with  $a_* = 0.7$ . The blue-dashed lines are for  $\eta = 0.0912$  and  $0.1221$ , which correspond, respectively, to the Novikov-Thorne radiative efficiency in Kerr background with  $a_* = 0.6$  and  $0.8$ . Right panel: as in the left panel for the frequency at the ISCO radius. The red-solid lines are for  $\Omega_{\text{ISCO}}/M = 0.1439$ , while the blue-dashed lines are for  $\Omega_{\text{ISCO}}/M = 0.1236$  (external lines) and  $0.1737$  (internal lines). In the Kerr background, these values of  $\Omega_{\text{ISCO}}/M$  correspond, respectively, to  $a_* = 0.7, 0.6$ , and  $0.8$ . See the text for more details.

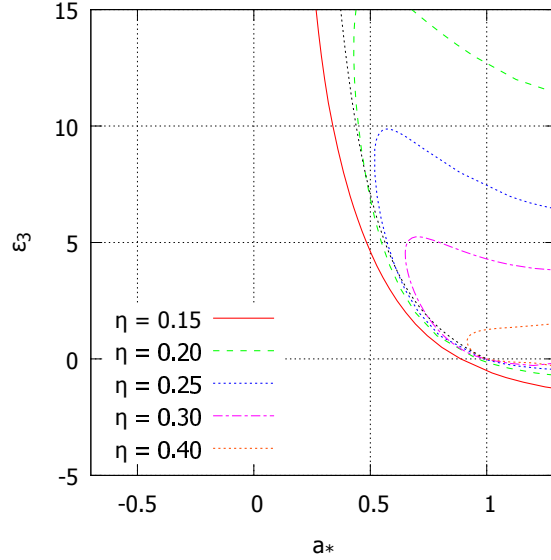


FIG. 7.— Some contour-levels showing the radiative efficiency in the Novikov-Thorne model  $\eta = 1 - E_{\text{ISCO}}$ . This is roughly the actual physical quantity measured in the continuum-fitting method, which can be later translated into a spin measurement in the Kerr background because there is a one-to-one correspondence between  $\eta$  and  $a_*$ . In the case of non-Kerr background, one finds an allowed region on the spin parameter–deformation parameter plane, since  $\eta = \eta(a_*, \epsilon_3)$ . Such an approximation works quite well for small viewing angles and low  $\eta$ , while there are some quantitative differences for large viewing angles and high  $\eta$ . See the text and Footnote 2 for more details.

- Jiang, J., Bambi, C., & Steiner, J. F. 2014, arXiv:1406.5677
- Johannsen, T., & Psaltis, D. 2011a, ApJ, 726, 11
- Johannsen, T., & Psaltis, D. 2011b, Phys. Rev. D, 83, 124015
- Johannsen, T., & Psaltis, D. 2013, ApJ, 773, 57
- Joshi, P. S., Malafarina, D., & Narayan, R. 2014, Classical and Quantum Gravity, 31, 015002
- Kalogera, V., & Baym, G. 1996, ApJ, 470, L61
- Kolehmainen, M., & Done, C. 2010, MNRAS, 406, 2206
- Kormendy, J., & Richstone, D. 1995, ARA&A, 33, 581
- Krawczynski, H. 2012, ApJ, 754, 133
- Li, L.-X., Zimmerman, E. R., Narayan, R., & McClintock, J. E. 2005, ApJS, 157, 335
- Li, Z., & Bambi, C. 2014, J. Cosmol. Astropart. Phys., 1, 41
- Li, Z., Kong, L., & Bambi, C. 2014, ApJ, 787, 152
- Liu, J., McClintock, J. E., Narayan, R., Davis, S. W., & Orosz, J. A. 2008, ApJ, 679, L37
- Liu, J., McClintock, J. E., Narayan, R., Davis, S. W., & Orosz, J. A. 2010, ApJ, 719, L109
- Maoz, E. 1998, ApJ, 494, L181
- McClintock, J. E., Narayan, R., Davis, S. W., et al. 2011, Classical and Quantum Gravity, 28, 114009
- McClintock, J. E., Narayan, R., & Rybicki, G. B. 2004, ApJ, 615, 402
- McClintock, J. E., Narayan, R., & Steiner, J. F. 2013, Space Sci. Rev., 73
- McClintock, J. E., Shafee, R., Narayan, R., et al. 2006, ApJ, 652, 518
- Middleton, M. J., Miller-Jones, J. C. A., & Fender, R. P. 2014, MNRAS, 439, 1740
- Morningstar, W. R., Miller, J. M., Reis, R. C., & Ebisawa, K. 2014, ApJ, 784, L18
- Narayan, R., & Heyl, J. S. 2002, ApJ, 574, L139
- Narayan, R., & McClintock, J. E. 2008, New Astronomy Reviews, 51, 733
- Novikov, I. D., & Thorne, K. S. 1973, in *Black Holes*, edited by C. De Witt and B. De Witt (Gordon and Breach, New York, US), 343
- Page, D. N., & Thorne, K. S. 1974, ApJ, 191, 49
- Pani, P., Barausse, E., Berti, E., & Cardoso, V. 2010, Phys. Rev. D, 82, 044009
- Psaltis, D., Perrodin, D., Dienes, K. R., & Mocioiu, I. 2008, Physical Review Letters, 100, 091101
- Remillard, R. A., & McClintock, J. E. 2006, ARA&A, 44, 49
- Rhoades, C. E., & Ruffini, R. 1974, Physical Review Letters, 32, 324
- Robinson, D. C. 1975, Physical Review Letters, 34, 905
- Shafee, R., McClintock, J. E., Narayan, R., et al. 2006, ApJ, 636, L113
- Shakura, N. I., & Sunyaev, R. A. 1973, A&A, 24, 337
- Steiner, J. F., McClintock, J. E., Orosz, J. A., et al. 2014, arXiv:1402.0148
- Steiner, J. F., McClintock, J. E., & Reid, M. J. 2012, ApJ, 745, L7
- Steiner, J. F., Reis, R. C., McClintock, J. E., et al. 2011, MNRAS, 416, 941
- Tsukamoto, N., Li, Z., & Bambi, C. 2014, J. Cosmol. Astropart. Phys., 6, 43
- Zhang, S. N., Cui, W., & Chen, W. 1997, ApJ, 482, L155